Scaling of slip avalanches in sheared amorphous materials based on large-scale atomistic simulations

Dansong Zhang, Karin A. Dahmen, and Martin Ostoja-Starzewski

Phys. Rev. E **95**, 032902 — Published 3 March 2017

DOI: 10.1103/PhysRevE.95.032902

Scaling of slip avalanches in sheared amorphous materials based on large-scale atomistic simulations

Dansong Zhang*
Department of Mechanical Science and Engineering
University of Illinois at Urbana-Champaign
Urbana, Illinois 61801, USA

Karin A. Dahmen†
Department of Physics
Institute for Condensed Matter Theory
University of Illinois at Urbana-Champaign
Urbana, Illinois 61801, USA

Martin Ostoja-Starzewski‡
Department of Mechanical Science and Engineering
Institute for Condensed Matter Theory and Beckman Institute
University of Illinois at Urbana-Champaign
Urbana, Illinois 61801, USA

Atomistic simulations of binary amorphous systems with over 4 million atoms are performed. Systems of two interatomic potentials of the Lennard Jones type, LJ12-6 and LJ9-6, are simulated. The athermal quasi-static shearing protocol is adopted, where the shear strain is applied in a stepwise fashion with each step followed by energy minimization. For each avalanche event, the shear stress drop ($\Delta\sigma$), the hydrostatic pressure drop ($\Delta\sigma_h$) and the potential energy drop (ΔE) are computed. It is found that, with the avalanche size increasing, the three become proportional to each other asymptotically. The probability distributions of avalanche sizes are obtained and values of scaling exponents fitted. In particular, the distributions follow a power-law, $P(\Delta U) \sim \Delta U^{-\tau}$, where ΔU is a measure of avalanche sizes defined based on shear stress drops. The exponent τ is 1.25± 0.1 for the LJ12-6 systems, and 1.15± 0.1 for the LJ9-6 systems. The value of τ for the LJ12-6 systems is consistent with that from an earlier atomistic simulation study by Robbins *et al.* [K. M. Salerno, C. E. Maloney, and M. O. Robbins, Phys. Rev. Lett. 109, 105703 (2012)], but the fitted values of other scaling exponents are different, which may be because the shearing protocol used here is different than in that study.

I. INTRODUCTION

Many systems in nature evolve in an intermittent fashion under external forcing [1]. Examples include earthquakes [2], biological extinction [3], magnetization [1], and fracture of porous materials [4], to name a few. One common feature of these phenomena is that the response of the systems is comprised of discrete events, termed "avalanches" or "bursts", which span a wide range of scales [1]. The same behavior is also observed in the plasticity of materials, evidenced by acoustic emission signals [5], or serrations in stress-strain curves [6, 7].

In crystalline materials, the "bursts" in dislocation motion are the cause of intermittency of plastic flows. More importantly, it is found that the motion of dislocations self-organizes to display a power-law probability distribution of avalanches sizes, $P(S) = S^{-\tau}$, where S is the magnitude of the avalanches given by the stress drops or the strain jump sizes. (Appendix B gives a list of symbols used in the paper.) The value of τ obtained from experiments on different crystals is $1.5 \sim 1.6$ [5, 8–10], consistent with the mean field exponent $\tau = 1.5$ [11, 12]. In particular, scaling collapses of the experimental data of slip avalanches at different stresses for slowly compressed nanopillars are consistent with the predictions of mean field theory [10–13]. Mesoscale models for crystal plasticity [14] also give similar results. Some two-dimensional (2D) discrete dislocation dynamics (DDD) simulations give slightly lower values for τ [15], while others give the mean field scaling behavior [16]. Phase field crystal simulations also support mean field scaling [17] and recent three-dimensional (3D) DDD simulations yield values close to the mean field scaling exponents [18].

Amorphous materials deform via a different mechanism than crystals. Instead of deforming via dislocation slips, in amorphous materials, plastic deformations are accommodated by the activation of shear transformation zones (STZs), where relative slips between atoms, or jumping of atoms to "vacancies" [19] take place. The operation of STZs gives rise to an intermittent plastic

* dzhang31@illinois.edu
† dahmen@illinois.edu
‡ martinos@illinois.edu

flow. Experiments by Sun *et al.* [6] on different types of metallic glasses showed that the probability distribution of stress drops in the stress-strain curves follows a power-law. The exponent τ ranges from 1.37 to 1.49, depending on the specific type of metallic glasses being tested. It is known that too low a time resolution can make the power law exponent appear lower than its real value [20]. Higher time resolution measurements on metallic glasses have been done by Wright *et al.* [21]. They were consistent with the mean field value of $\tau = 1.5$ and the scaling behavior of about 12 different statistical quantities agreed with predictions of mean field theory [22], providing exceptionally strong confirmation for the mean field theory predictions in bulk metallic glasses. Another support for the mean field results comes from a spring-lattice-based model recently proposed in Ref. [23], which gave $\tau = 1.5 \pm 0.1$ for anti-plane deformations of a 2D spring lattice. Values of τ close to the mean field prediction are also obtained from the simulations in Ref. [24]. However, some simulations of mesoscale models in 2D, i.e. for sheared thin sheets of bulk metallic glasses, in the literature produce different results. A 2D mesoscale lattice model of Talamali *et al.* [25] gives $\tau = 1.25 \pm 0.05$, while a later simulation study based on the same model gives a slightly different value of $\tau \approx 1.35$ [26]. Simulations of a recent elasto-plastic model proposed by Lin *et al.* [27] predict that $\tau = 1.36$ for 2D and $\tau = 1.45$ for 3D. The latter result in 3D is very close to the mean field exponent of 1.5. The deviation for simulations in 2D is not so surprising as renormalization group calculations predict that for 1D shear bands in 2D systems, one expects corrections to the mean field theory results. In contrast, for 2D shear bands in 3D solids, the renormalization group predicts mean field scaling behavior (up to small logarithmic corrections) [12, 28]. A mean field model has recently been suggested to study the density of shear transformation zones in simulations of amorphous solids during steady state deformation [29].

Atomistic simulation is an important tool for the study of avalanche behavior in amorphous materials, because it can be used to test some of the assumptions that the coarse grained models are based on. However, atomistic simulations have assumptions of their own that need to be tested as well. The dependence of avalanche size on system size is investigated by many researchers using atomistic simulation [30–33]. Maloney and Lemaître [30] simulated the quasi-static shear deformation of a 2D amorphous system with the atomic interaction governed by a soft-particle potential, where a power-law distribution of energy drops during avalanches was observed: $P(\Delta E) = \Delta E^{-\tau'}$. (The exponent τ is primed, in order to differentiate from the τ obtained from measures of stress drops.) It was found that the exponent τ' decreases from 0.7 to 0.5 as the system size increases and, in addition, a linear geometric structure of avalanches is observed, which explains their finding that avalanche sizes scale linearly with system width, $S \sim L$. The scaling of avalanche size with system size, $S \sim L^{\alpha}$, is also the focus of the 2D study by Lerner *et al.* [31] and the 3D study by Bailey *et al.* [33], but different values for the scaling exponent α were obtained. 3D simulations are also performed by Lerner *et al.* [32] on three different atomic systems. The probability distributions of energy drops and stress drops are virtually the same for those different systems. A comprehensive study of the scaling properties of avalanches in amorphous samples is done by Salerno *et al.* [34, 35]. Systems with up to 1 million atoms are used. A viscous damping is introduced, which can be tuned to model three different cases: overdamped, underdamped and critically damped. The values of $\tau(\tau')$ and avalanche finite-size-scaling exponents are obtained. One important issue with atomistic simulation is how to simulate a quasi-static deformation. In Salerno's study, the samples are sheared at a fixed strain rate, but shearing is paused whenever the kinetic energy of the system shoots up (a sign of avalanches) and resumed when the kinetic energy is dissipated. Another way of modeling quasi-static shear reported in the literature, which is more common and straightforward, is to increase the strain incrementally with each strain increment followed by energy minimization [30, 32, 36–38]. Since energy is always minimized before the next strain increment is applied, this shearing protocol corresponds to the overdamped case in Refs. [34, 35]. It is necessary to check whether both methods produce the same results. However, except Ref. [30] mentioned above, we have found no atomistic simulations that adopt the second protocol of shearing to obtain a measure of $\tau(\tau')$. In addition, the effect of step size on the resultant statistics has not yet been discussed.

The study reported in this paper adopts the second method with small strain steps to simulate quasi-static simple shear deformation of amorphous samples in 2D. The largest systems contain $4,096,000$ atoms, which are larger than the systems in all previous studies of avalanches in amorphous materials in the literature. The reason for using such a big system size is to rule out possible finite size effects on the scaling properties. In addition, two types of atomic systems are simulated, in order to check whether the scaling properties are independent of the interatomic potential.

The paper is organized as follows. Section 2 briefly describes the simulation method. In Section 3, the relationship between the shear stress drop, the hydrostatic pressure drop and the potential energy drop for each avalanche event is studied. The probability distributions of avalanche sizes are plotted. Finally, the values of τ and finite-size-scaling exponents are extracted from the probability distributions. Readers can refer to Table IV for a list of values of the exponents.

II. METHOD

The samples are 2D, containing two different atom species, A and B, with two atomic systems (I and II)

studied. The potential I is a smoothed Lennard-Jones potential [35].

$$E_{ij} = 4E_0 \left[\left(\frac{a_{ij}}{r} \right)^{12} - \left(\frac{a_{ij}}{r} \right)^{6} \right] + E_c \qquad (r < 1.2a_{ij}) \quad (1)$$

where E_0 is the characteristic energy, E_c is an energy offset, a_{ij} is the "interaction length" between atoms of type i and of type j. The "interaction length" between two atoms A ($a_{\rm AA}$) is the characteristic length unit a, the "interaction length" between two atoms B ($a_{\rm BB}$) is $0.6a$. The mixed "interaction length" $a_{\rm AB} = a_{\rm BA} = 0.8a$. The systems are non-dimensionalized with energy unit ϵ and length unit a. In the region where $1.2a_{ij} < r < 1.5a_{ij}$, atomic interactions are approximated by a quartic smoothing function, to make sure the energy, force, and the first derivative of force are continuous at both the inner cutoff radius $1.2a_{ij}$, and the outer cutoff radius $1.5a_{ij}$. Outside of the outer cutoff radius, the interatomic energy and force are zero. The number of atoms A to the number of atoms B is $\left(1+\sqrt{5}\right)/4$, the value used in Refs. [34, 35].

The potential II is a Lennard-Jones 9-6 potential,

$$E_{ij} = 4E_0 \left[\left(\frac{a_{ij}}{r} \right)^{9} - \left(\frac{a_{ij}}{r} \right)^{6} \right] + E_c \qquad (r < r_c) \quad (2)$$

The definitions and values of the parameters are listed in Table I. The values are chosen such that the potential curves are comparable to that used in [39]. The number of atoms A relative to the number of atoms B is 43 : 57 [39]. According to the mean field theory, the scaling properties of avalanches are universal in nature [11, 12]. We use a potential that differs from those used in other studies [30, 31, 35, 40] (which also differ amongst themselves with respect to the potentials they use). Thus, we are further testing whether the simulation results are universal with respect to the choice of potential. Potentials that correspond to real amorphous materials, e.g. effective medium theory potentials [41] or embedded atom method potentials [42], may be used in future studies, although the maximum system size might be limited due to the more expensive computational cost.

The molecular dynamics code LAMMPS is used to perform the simulations. Periodic boundary conditions are applied on all sides of the samples [34, 35, 37, 40, 43]. For both systems, the initial samples are prepared by a melt-quench procedure [31, 37, 44, 45], i.e. the systems are first heated up to well above the melting point and then cooled down very fast, with a quenching rate of $\sim 2 \times 10^{12}$ K/s to a temperature close to 0K ($\sim 1/1,000$ of the initial temperature). A Nosé-Hoover thermo/barostat [46] is used to control the temperature and the pressure during quenching, while the pressure is controlled to be zero. Finally, potential energy minimization using the conjugate gradient method is performed on the samples to drive the systems to an equilibrium state. Samples with different numbers of atoms are obtained. For each system, different strain increments are used. The numbers of realizations for each combination of system size and strain increment are listed in Table II and Table III. Note that the smallest strain increment is much smaller than those in [33, 37], and is comparable with the smallest ones in [31]. For potential I, the largest samples have $4,096,000$ atoms, considerably larger than the samples in most previous studies of this kind [32–34, 37], and also 4 times larger than the largest atomistic simulations we have seen so far in this area [34]. For potential II, the largest samples have $512,000$ atoms. One sample using potential I with $8,000$ atoms is shown in Figure 1.

TABLE I: Parameters for potential II (c.f. Eq. (2)). There are two types of atoms: A and B. As a result, there are three different types of atom pairs: A-A (a pair of atoms A), A-B (a pair of one atom A and one atom B), and B-B (a pair of atoms B). The parameters in Eq. (2) are different for the three different atom pairs, as listed in the table. E_0 is the characteristic energy, E_c is an energy offset. a_{ij} is the "interaction length" between atoms of type i and of type j. r_c is the cutoff distance.

Pair	E_0 (eV)	a_{ij} (Å)	E_c (eV)	r_c (Å)
A-A	0.75250	2.87048	0.032138	6.000
A-B	0.59915	2.60136	0.021667	5.600
B-B	0.45251	2.32493	0.014511	5.112

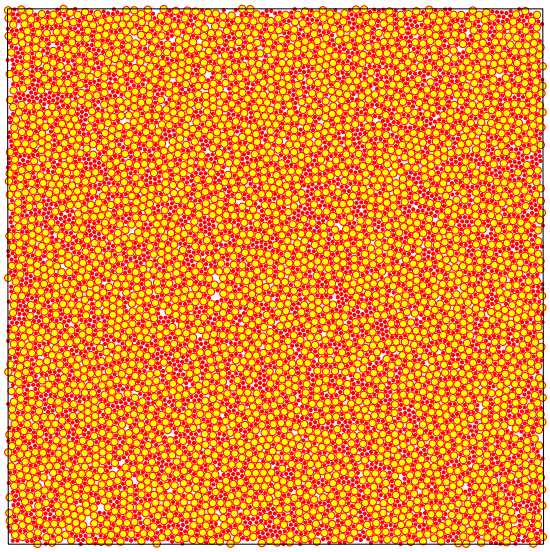

FIG. 1: (Color online) A sample with 8,000 atoms using potential I (big: atom A, small: atom B)

Simple shear deformation is then applied incrementally on the samples, and, after each shear strain increment, the box is held fixed and the potential energy is minimized using the aforementioned conjugate gradient algorithm before the next strain increment is applied. Since no thermal vibration is considered, the model corresponds to a zero temperature limit. If the strain incre-

TABLE II: Number of realizations of different combinations of system size N (number of atoms) and strain increment $\Delta\epsilon$ (increase of shear strain in each step) using the LJ12-6 potential (Cells that are blank mean no realizations)

N	$\Delta\epsilon$					
	1×10^{-4}	5×10^{-5}	2×10^{-5}	1×10^{-5}	5×10^{-6}	2×10^{-6}
8,000	10	10	10	10	10	10
16,000	10	10	10	10	10	10
32,000	10	10	10	9	8	5
64,000	8	6	8	8	10	5
128,000		10	10	10	10	3
256,000				2	4	2
512,000				4	4	2
1,024,000				2	2	
4,096,000					3	

TABLE III: Number of realizations of different combinations of system size N (number of atoms) and strain increment $\Delta\epsilon$ (increase of shear strain in each step) using the LJ9-6 potential (Cells that are blank mean no realizations)

N	$\Delta\epsilon$					
	1×10^{-4}	5×10^{-5}	2×10^{-5}	1×10^{-5}	5×10^{-6}	2×10^{-6}
4,000	31	30	40	30	20	20
8,000	30	30	40	30	20	20
16,000	30	30	40	30	30	20
32,000	20	30	40	30	20	10
64,000		10	10	10	9	
128,000					10	
256,000					4	
512,000					2	

ment is small enough, we are able to approach the limit of zero strain rates. It was pointed out that many granular materials and glassy systems can be considered athermal [37]. This approach has also been widely used in the study of metallic glasses at slow strain rates [38, 47, 48]. The effect of strain increment is discussed below. The samples lie in the xy-plane, and simple shear is applied in the positive x-direction.

III. RESULTS

A. Stress and energy change during avalanches

Figure 2 shows examples of stress components and potential energy when the samples are sheared. The deformation is initially elastic, and then turns into a plastic regime full of serrations, which are signs of slip avalanches. No fracture was observed in the samples throughout the deformations. Only the avalanche events after the stress has stabilized are used for the following analyses.

Many studies have reported that the plastic deformation of metallic glasses is associated with a free volume increase, or local dilation [49–54]. Our simulation is able to confirm this by tracking the change of hydrostatic stress

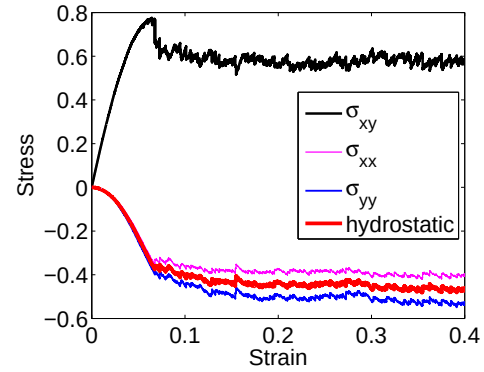

(a)

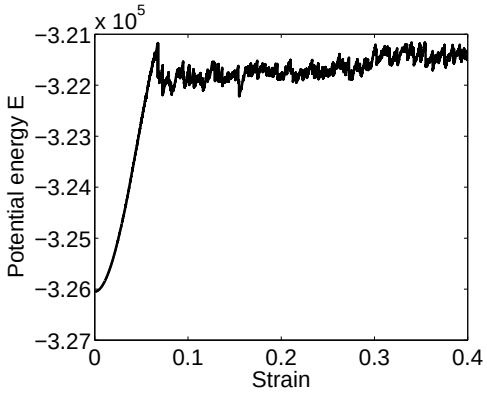

(b)

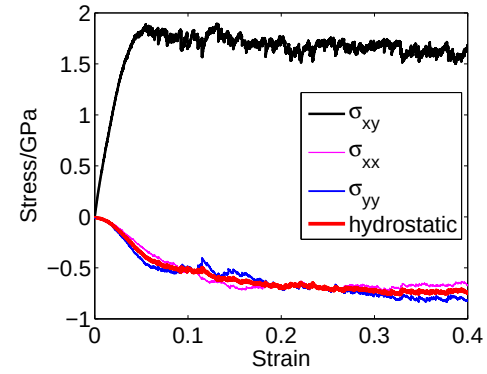

(c)

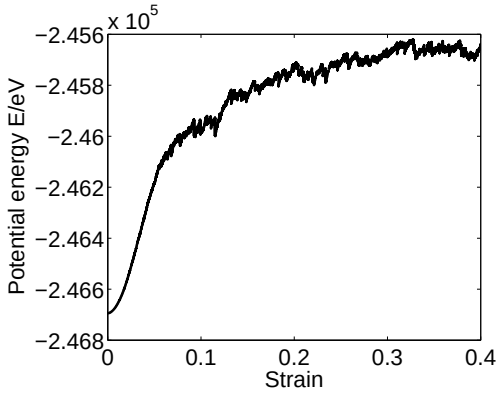

(d)

FIG. 2: (Color online) Stress vs. strain and potential energy vs. strain of (a-b)potential I and (c-d)potential II. The number of atoms is 256, 000.

during shear (Figure 2, similar to those obtained from the 3D simulation of Cu-Zr amorphous alloys by Ogata *et al.* [38]). As we increase the shear strain, the magnitude of hydrostatic stress is also increasing. Because the area of the sample is conserved during simple shear, such a change in hydrostatic stress implies a tendency of the material to dilate, pressing harder and harder on the boundaries. An actual increase in the area of the system would be observed if there were free-surface boundaries. To avoid confusion, we use the term "hydrostatic pressure" to refer to the absolute value of the hydrostatic stress.

The hydrostatic pressure drop $\Delta\sigma_h$ and the shear stress drop $\Delta\sigma$ for an avalanche event occurring in the i-th shear step are defined as follows:

$$\Delta\sigma_h = (\sigma_h)_i - (\sigma_h)_{i+1} \tag{3}$$

$$\Delta\sigma = \sigma_i - \sigma_{i+1} \tag{4}$$

where $(\sigma_h)_i$ and $(\sigma_h)_{i+1}$ are the hydrostatic pressure before and after the i-th shear step, respectively; and σ_i and σ_{i+1} are the shear stress before and after the i-th shear step, respectively. The values of $\Delta\sigma_h$ and $\Delta\sigma$ for each avalanche event are plotted with scattered crosses in Figure 3(a). The events are then logarithmically binned according to their values of $\Delta\sigma$ and the average of the values of $\Delta\sigma_h$ are computed in each bin, to get an average hydrostatic pressure drop $\langle\Delta\sigma_h\rangle$ vs. $\Delta\sigma$. It is seen that with increasing $\Delta\sigma$, the data points become less scattered and, more importantly, $\langle\Delta\sigma_h\rangle$ tends to become linear in $\Delta\sigma$ asymptotically. It is also worth noting that, when the strain increment $\Delta\epsilon$ is reduced, the distribution of the data points are not altered except that more data points are added to the left due to more small events being captured. In addition, the $\langle\Delta\sigma_h\rangle$ vs. $\Delta\sigma$ curves for different system sizes are compared in Figure 4(a). The curves collapse for large events, suggesting that the relationship between $\langle\Delta\sigma_h\rangle$ and $\Delta\sigma$ is not affected by the system size.

Similarly, we can define the energy drop in each avalanche event as

$$\Delta E = E_i - E_{i+1} \tag{5}$$

where E_i and E_{i+1} are the potential energy of the system before and after the i-th shear step, respectively. Similar analysis to the above can be applied to the relationship between ΔE and $\Delta\sigma$ and the results are shown in Figure 3(b). Again, we see the data points become less scattered, and $\langle\Delta E\rangle$ becomes linear in $\Delta\sigma$ asymptotically, as the event size increases. Alternatively, shear stress drop and potential energy drop can be defined as

$$\Delta\sigma = \sigma_i + \mu\Delta\epsilon - \sigma_{i+1} \tag{6}$$

$$\Delta E = E_i + A\sigma_i\Delta\epsilon - E_{i+1} \tag{7}$$

where μ is the shear modulus of the system measured from the elastic portion of the stress-strain curve, and A is the area of the system [33]. $\sigma_i + \mu\Delta\epsilon$ is what the stress should be after the strain increment $\Delta\epsilon$ if there were no slips, whereas σ_{i+1} is the actual stress after the strain increment. Therefore, the $\Delta\sigma$ given by Eq. (6) is purely the change in stress brought about by the slips. Similarly, since $A\sigma_i\Delta\epsilon$ is the external work during the strain increment $\Delta\epsilon$, $E_i + A\sigma_i\Delta\epsilon$ is what the potential energy should be after the strain increment if there were no slips, whereas E_{i+1} is the actual potential energy after the strain increment. Therefore, the ΔE given by Eq. (7) is the potential energy dissipated during the slip. Moreover, the plastic strain accumulated during the slip, $\Delta\epsilon_{pl}$, is equal to $\Delta\sigma/\mu$, if we use $\Delta\sigma$ defined by Eq. (6) [33]. Due to the reasons above, we consider Eqs. (6) and (7) to be better characterizations of the avalanche sizes than Eqs. (4) and (5). While plotting the relationship between hydrostatic pressure drops and shear stress drops, we use Eq. (4) to compute the shear stress drops. The reason is because the way of computing $\Delta\sigma$ should be consistent with that of $\Delta\sigma_h$, and a correction term for $\Delta\sigma_h$ that is analogous to $\mu\Delta\epsilon$ is hard to determine due to the fact that hydrostatic pressure does not increase linearly with strain during the elastic deformation (Figure 2). But the relative error of neglecting the correction terms $\mu\Delta\epsilon$ and $A\sigma_i\Delta\epsilon$ is only significant for small events. Figure 3(c) shows the scatter plots for ΔE and $\Delta\sigma$, based on the definition from Eqs. (6) and (7). It can be seen that only the data points for small events are redistributed, which does not affect our conclusions above for large events.

The effect of system size on the relationship between $\langle\Delta E\rangle$ and $\Delta\sigma$ is shown in Figure 4(b-c). As the system size increases, $\langle\Delta E\rangle$ approaches a linear dependence on $\Delta\sigma$ more quickly. More importantly, when $\langle\Delta E\rangle$ is scaled by the area of the system L^2, the right hand side of all the curves collapse, i.e. $\langle\Delta E\rangle \sim \Delta\sigma L^2$ for large events. In summary, for large events,

$$\Delta\sigma_h \sim \frac{\Delta E}{L^2} \sim \Delta\sigma \tag{8}$$

B. Probability distributions of avalanche sizes

For the reasons mentioned above, we use Eq. (6) to define $\Delta\sigma$ and Eq. (7) to define ΔE, for the following analysis. Similar to Ref. [34], we define

$$\Delta U = \frac{\langle\sigma\rangle\Delta\sigma}{\mu}A \tag{9}$$

where $\langle\sigma\rangle$ is the steady-state shear stress. From this definition,

$$\Delta U \sim \frac{\Delta\sigma}{\mu}A \sim \Delta\epsilon_{pl} \tag{10}$$

where $\frac{\Delta\sigma}{\mu}A$ is a 2D version of the "*slip volume*" defined in [33], which can be considered as "*a measure of the*

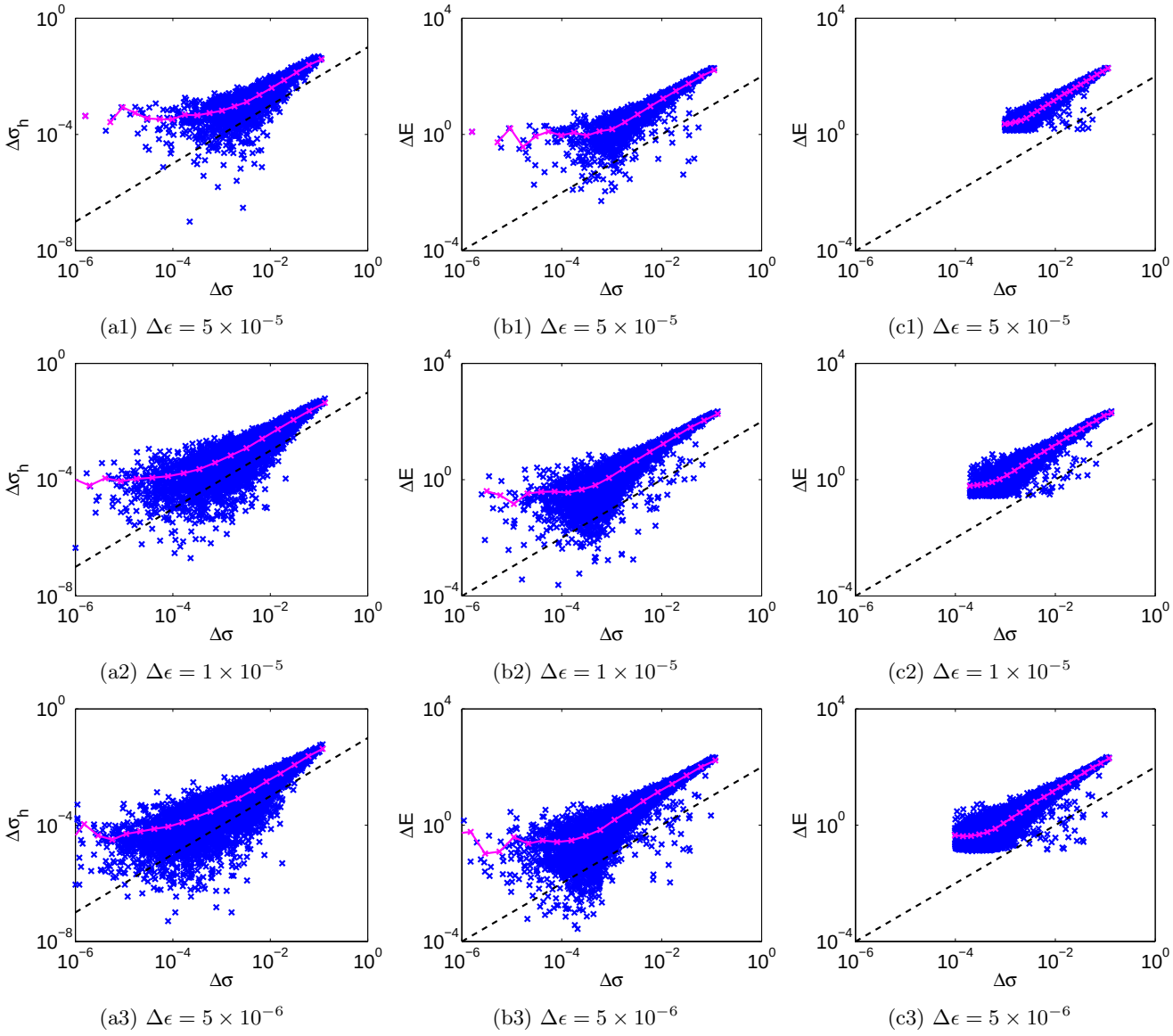

FIG. 3: (Color online) Relationship between hydrostatic pressure drop ($\Delta\sigma_h$), shear stress drop ($\Delta\sigma$) and energy drop (ΔE) for potential I. The number of atoms is 64,000. The strain increments are labeled by the subcaptions. Each blue cross represents a single event. The red curves are obtained by first logarithmically binning the events according to their stress drops, and then averaging the hydrostatic pressure drops (for (a)) or the energy drops (for (b-c)) within each bin. The black dashed lines have a slope of 1. $\Delta\sigma_h$ is defined by Eq. (3). In (b), $\Delta\sigma$ and ΔE are calculated using Eqs. (4) and (5), respectively. In (c), $\Delta\sigma$ and ΔE are calculated using the corrected formulas Eqs. (6) and (7), respectively.

number of elementary transformations which contribute to the macroscopic stress relaxations". ΔU can then be understood as an estimate of the work by the external stress on the "*slip volume*". ΔU and ΔE both have the unit of energy. In the following analysis, we will focus on the probability distributions of ΔU and ΔE, which are denoted by $P(\Delta U)$ and $P(\Delta E)$, respectively.

To determine the distributions, we first count the number of events in each bin, and then divide it by the width of the bin. The entire distributions are further divided by the width of the strain interval within which slip avalanche events were counted. Therefore, $P(\Delta U)\, d(\Delta U)$ is the number of events that fall in the range $[\Delta U, \Delta U + d(\Delta U)]$ per unit strain interval. Similarly, $P(\Delta E)\, d(\Delta E)$ is the number of events that fall in the range $[\Delta E, \Delta E + d(\Delta E)]$ per unit strain interval. We have verified that the length and position of the strain interval do not affect the final distributions as long as the interval lies in the plastic regime. The probability distributions at different strain increments are plotted in Fig-

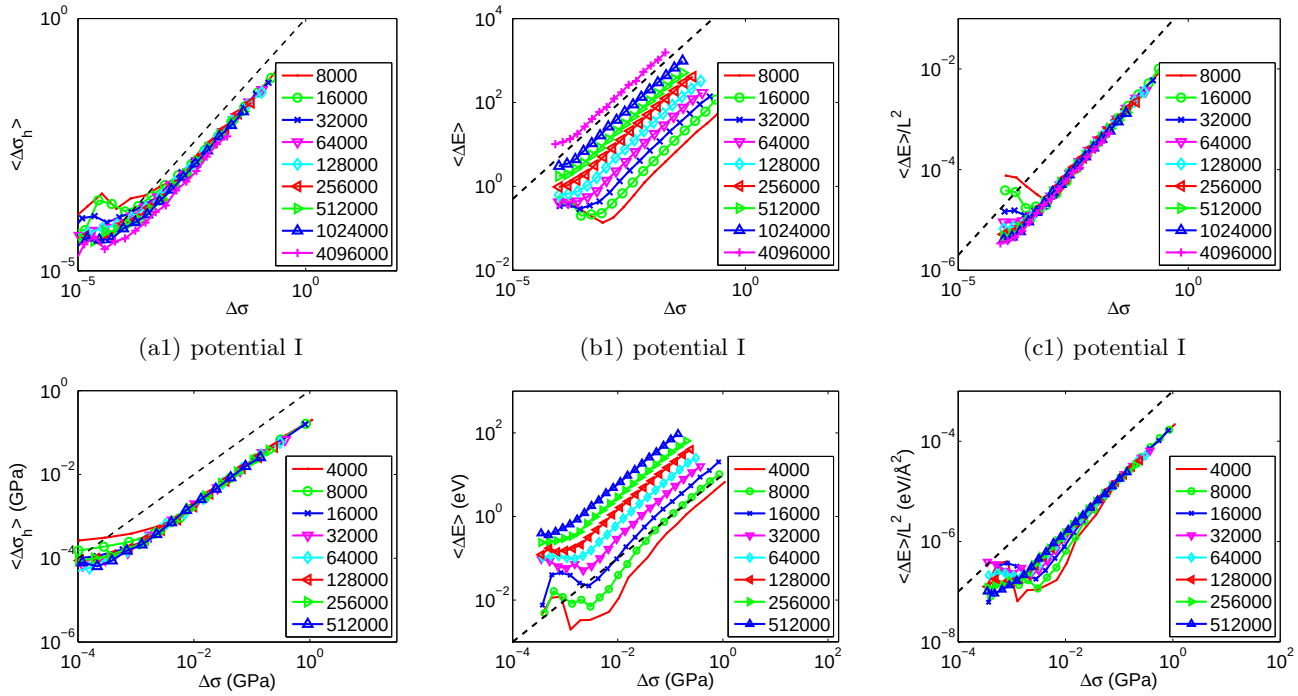

FIG. 4: (Color online) (a)Average hydrostatic pressure drop ($\langle\Delta\sigma_h\rangle$), (b)average energy drop ($\langle\Delta E\rangle$) and (c)scaled average energy drop ($\langle\Delta E\rangle/L^2$) for potential I and potential II with different system sizes. L is the side length of the system. The strain increment is $\Delta\epsilon = 5\times10^{-6}$. In each subfigure, the curves are obtained by first logarithmically binning the events according to their stress drops, and then averaging the hydrostatic pressure drops (for (a)) or the energy drops (for (b-c)) within each bin. $\Delta\sigma_h$ is defined by Eq. (3). In (b-c), $\Delta\sigma$ and ΔE are calculated using the corrected formulas Eqs. (6) and (7), respectively. The black dashed lines have a slope of 1.

ure 5. It is seen that reducing the strain increment simply extends the curves further to the left because smaller events are better captured, while the right portion of the curves remain unaffected. We choose a strain increment of 5.0×10^{-6} and plot the distributions as the system size varies (Figure 6).

For potential I, the curves of $P(\Delta U)$ follow a power law, with an exponential cutoff on the right. The exponent of the power-law is estimated to be $\tau = 1.25\pm0.1$.

For potential II, the curves of $P(\Delta U)$ have a "hump" on the left, but the middle part also follows a power law. The exponent of the power-law is estimated to be $\tau = 1.15\pm0.1$.

In contrast to $P(\Delta U)$, the curves of $P(\Delta E)$ cannot be fit with a power law with high certainty. A similar issue has been reported in Ref. [34] with the distributions of ΔE, where the distributions of ΔU (a quantity proportional to ΔU, to be exact) were used to determine the power law exponent of the avalanches.

The following finite-size scaling is performed on the original distributions:

$$\frac{P(\chi)}{L^{\beta}} = f\left(\frac{\chi}{L^{\alpha}}\right) \tag{11}$$

where χ represents either ΔU or ΔE [34]. The scaled distributions are shown in Figure 7. For potential I, $P(\Delta U)$ shows a good collapse under the scaling when $\alpha = 1.25$ and $\beta = -0.5$. For potential II, $\alpha = 1.2$ and $\beta = -0.3$ gives a good collapse of $P(\Delta U)$ curves. On the other hand, the curves of $P(\Delta E)$ cannot be collapsed closely under finite-size scaling neither for potential I nor for potential II, because the shapes of the curves change slightly with the system size.

Another scaling property that is investigated is the scaling of the number of slip events of a given size with the system size. Salerno *et al.* [34, 35] found the scaling to be subextensive, i.e. the number of events does not increase linearly with the number of particles, which scales with L^D, where D is the dimension of the system. Instead, the number of events scales as L^{γ}, with $\gamma < D$. To get γ, we scale the original curves of $P(\chi)$ by L^{γ}. The objective is to find a proper γ such that the power-law portions of the curves collapse. The scaled curves are shown in Figure 8. With potential I, for $P(\Delta U)$, $\gamma = 1.05\pm0.10$ and for $P(\Delta E)$, $\gamma = 1.00\pm0.05$. As expected, these two γ's have overlapping error bars. With potential II, $\gamma = 1.15\pm0.10$ for both $P(\Delta U)$ and $P(\Delta E)$. A full list of all the scaling exponents from our simulations, together with the values from Refs. [34, 35] that correspond to the 2D overdamped case, is shown in Ta-

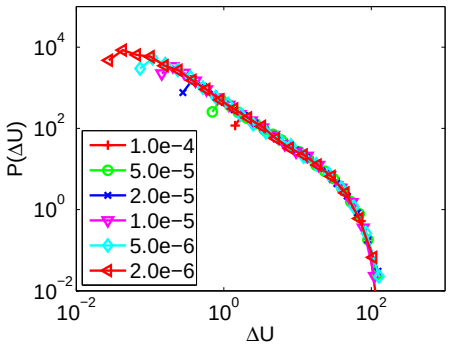

(a) potential I

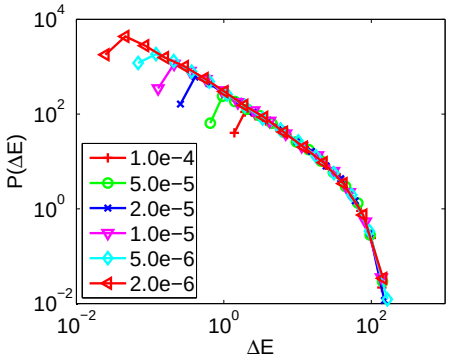

(b) potential I

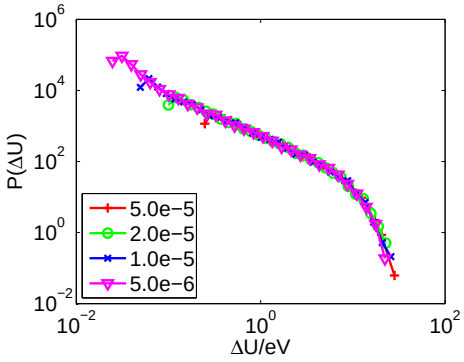

(c) potential II

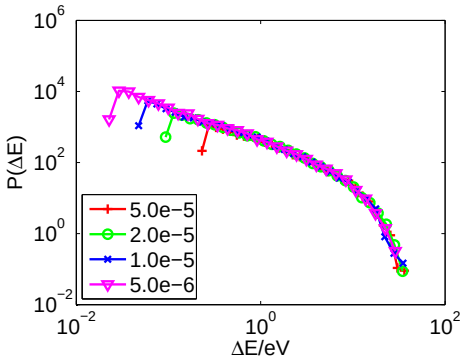

(d) potential II

FIG. 5: (Color online) Original $P(\Delta U)$ (probability distribution of ΔU, with ΔU defined in Eq. (9)) and $P(\Delta E)$ (probability distribution of energy drop ΔE, with ΔE defined in Eq. (7)) at different strain increments, which are indicated by the legends. The number of atoms in each system is 64,000.

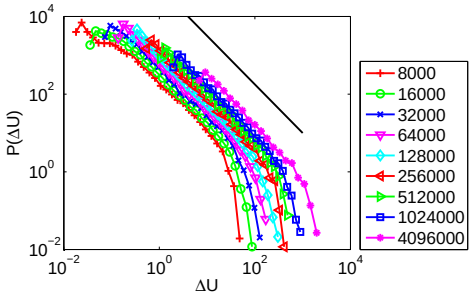

(a) potential I

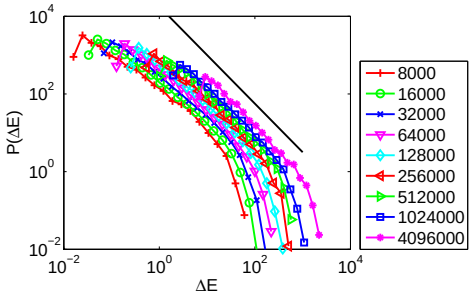

(b) potential I

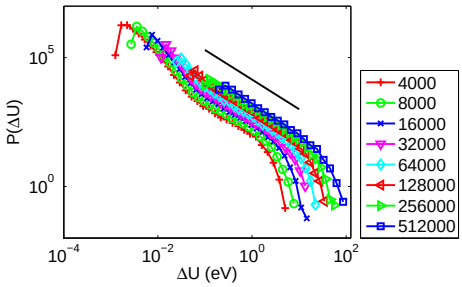

(c) potential II

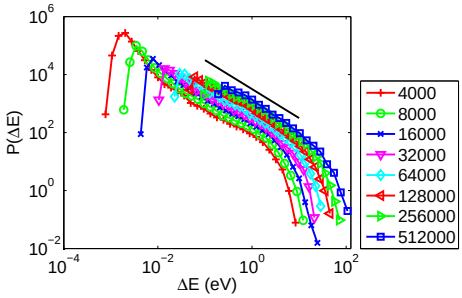

(d) potential II

FIG. 6: (Color online) Original $P(\Delta U)$ (probability distribution of ΔU, with ΔU defined in Eq. (9)) and $P(\Delta E)$ (probability distribution of energy drop ΔE, with ΔE defined in Eq. (7)). The system sizes, given in the numbers of atoms, are indicated by the legends. The strain increment is 5×10^{-6}. The slopes of the straight reference lines are -1.25 in (a-b), -1.15 in (c) and -1.0 in (d). Plotting the reference lines in (b) and (d) is just to show the rough trend.

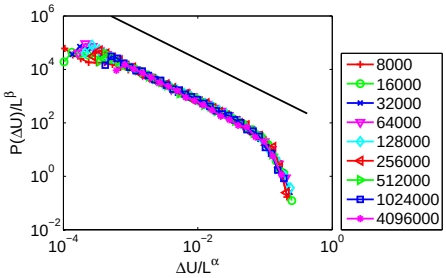

(a) potential I

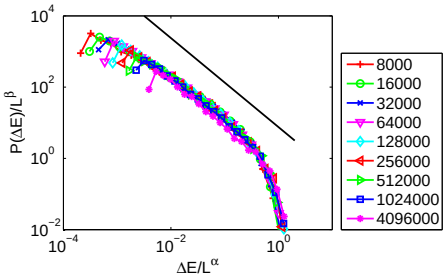

(b) potential I

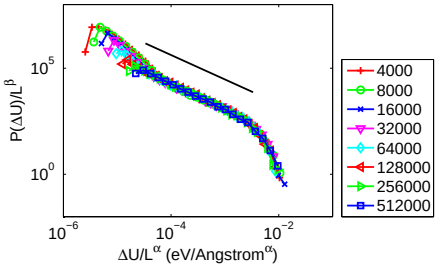

(c) potential II

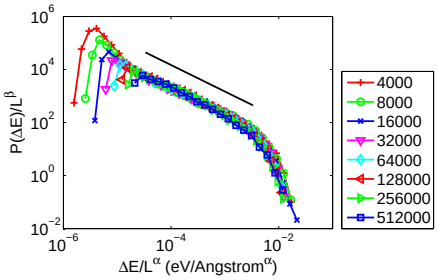

(d) potential II

FIG. 7: (Color online) Finite-size scaled $P(\Delta U)$ (probability distribution of ΔU, ΔU defined in Eq. (9)) and $P(\Delta E)$ (probability distribution of energy drop ΔE, ΔE defined in Eq. (7)). L is the side length of the system. The definition of the finite-size scaling is given in Eq. (11). The system sizes, given in the numbers of atoms, are indicated by the legends. The strain increment is 5.0×10^{-6}. The slopes of the straight reference lines are -1.25 in (a-b), -1.15 in (c) and -1.0 in (d). Plotting the reference lines in (b) and (d) is just to show the rough trend, since the shapes of the curves cannot be fit with a straight line. In (a), $\alpha = 1.25$ and $\beta = -0.5$. In (b), $\alpha = 1$ and $\beta = 0$. In (c), α=1.2 and $\beta = -0.3$. In (d), $\alpha = 1.2$ and $\beta = -0.05$. A better collapse in (b) and (d) cannot be achieved by choosing different values for α and β.

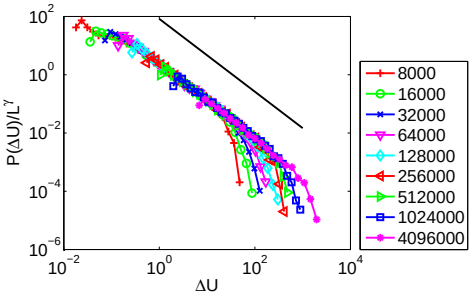

(a) potential I

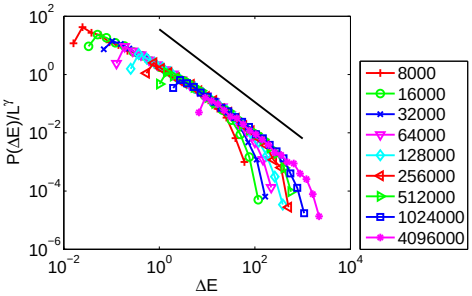

(b) potential I

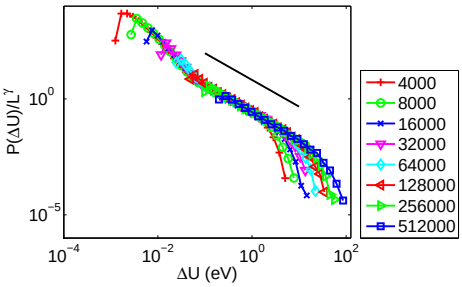

(c) potential II

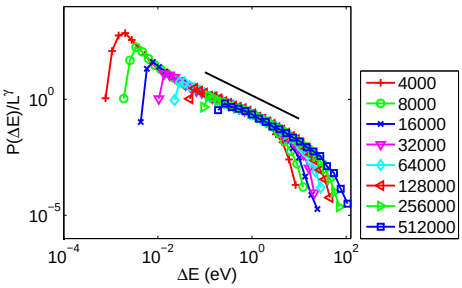

(d) potential II

FIG. 8: (Color online) $P(\Delta U)$ (probability distribution of ΔU, ΔU defined in Eq. (9)) and $P(\Delta E)$ (probability distribution of energy drop ΔE, ΔE defined in Eq. (7)) scaled by L^{γ}. L is the side length of the system. The system sizes, given in the numbers of atoms, are indicated by the legends. The strain increment is 5.0×10^{-6}. γ is 1.05 for (a), 1.00 for (b), and 1.15 for (c-d). The slopes of the straight reference lines are -1.25 in (a-b), -1.15 in (c) and -1.0 in (d). Plotting the reference lines in (b) and (d) is just to show the rough trend.

ble IV.

In Refs. [34, 35], two relations between the scaling exponents are proposed: $\gamma = \beta + \alpha\tau$ and $\beta = 2 - 2\alpha$. The first relation is derived from the definitions of the scaling exponents. The second one is derived based on the energy conservation at steady-state shear. We can see that all the exponents in Table IV satisfy these relations approximately. In Appendix A, a scaling relation that involves the "waiting time" , which is defined as the additional strain required to trigger the next avalanche after one avalanche is observed, is proposed and it is supported by scaling collapses of avalanche data from our simulations. Furthermore, it is seen that the value of τ from our simulations using potential I is close to those from Refs. [34, 35], which is expected, since the same interatomic potential is used. However, our simulations give values of α, β and γ different than those in Refs. [34, 35] and it is likely so because our quasi-static shearing protocol is different than that in Refs. [34, 35]. In our simulation, we apply strain increment $\Delta\epsilon$, and minimize the potential energy. This is equivalent to applying a sudden increase in strain, and then giving the system enough time to relax to the nearest stable state. When the strain is being applied, the system is not allowed to respond. But in Refs. [34, 35], molecular dynamics simulation is used between adjacent avalanches. i.e. when the strain is being applied, the system is responding simultaneously. Therefore, even though both methods are approximating quasi-static deformation, the difference in the way of applying strains can lead to different system behavior. Other values of α are found in the literature based on slightly different interpretations of the exponent. Lerner *et al.* [31] found the average avalanche size to scale with the system size as $L^{0.74}$ from their atomistic simulation. But the system sizes are much smaller than ours. Lin *et al.* used an elasto-plastic model to predict the scaling of the cutoff avalanche size, $S_c \sim L^{d_f}$, where the value of d_f is reported to be 0.77 or 0.71 in Ref. [55] and 1.1 in Ref. [27]. Finally, the error bars of the two τ's corresponding to the two potentials overlap, therefore, within error bars, our simulations are consistent with the prediction that τ is independent of the potential.

IV. CONCLUSIONS

In this study, the simple shear deformation of two different binary amorphous systems is simulated. An athermal quasi-static shearing protocol is used, where shear strains are applied stepwise, with each shearing step followed by energy minimization. The LJ12-6 systems have a maximum of $4,096,000$ atoms, and the LJ9-6 systems have a maximum of $512,000$ atoms. Each avalanche event is accompanied by a shear stress drop ($\Delta\sigma$), a hydrostatic pressure drop ($\Delta\sigma_h$) and a potential energy drop (ΔE). For large avalanche events, the three are proportional to each other. In order for the deformation to be quasi-static, the strain increment in each step needs to be small enough. To this end, a variety of strain increments are tested. It is then shown that reducing the strain increment does not affect the probability distributions of avalanches except that a larger number of smaller events are captured. In addition, for each avalanche event, a measure of the avalanche size, ΔU, is computed based on the shear stress drop, $\Delta\sigma$. It is proportional to the shear stress drop $\Delta\sigma$, and the plastic strain accumulated during the avalanche. The probability distributions of ΔU are found to follow a power law. The exponent τ of the power-law is 1.25 ± 0.1 for the LJ12-6 systems, which is consistent with $\tau = 1.3 \pm 0.1$ in Ref. [34] and $\tau = 1.25 \pm 0.05$ in Ref. [35] obtained from simulations of 2D overdamped systems with up to 1 million atoms. For the LJ9-6 systems, τ is found to have a slightly lower value of 1.15 ± 0.1. But within overlapping error bars, our simulations are consistent with the prediction that τ is universal, i.e. independent of the interatomic potential.

Finally, the probability distributions of ΔU of different system sizes can be collapsed under a proper finite-size scaling, $P(\Delta U)/L^{\beta} = f(\Delta U/L^{\alpha})$, where $\alpha = 1.25 \pm 0.05$ and $\beta = -0.5 \pm 0.1$ for the LJ12-6 systems, and $\alpha = 1.2 \pm 0.1$ and $\beta = -0.3 \pm 0.1$ for the LJ9-6 systems. The scaling exponents α and β for the LJ12-6 systems are different than those in Refs. [34, 35], which are $\alpha = 0.9 \pm 0.05$ and $\beta = 0.2 \pm 0.1$, even though the same interatomic potential is used. It is then likely that the difference in the scaling exponents results from the difference between the shearing protocols in this study and in Refs. [34, 35]. Comparative studies of these two shearing protocols are needed in the future to clarify this issue. Despite the discrepancy above, both the exponents from our simulations and those from Refs. [34, 35] satisfy the two relations, $\gamma = \beta + \alpha\tau$ and $\beta = 2 - 2\alpha$.

ACKNOWLEDGMENTS

K.A.D. acknowledges helpful discussions with C.E. Maloney and M.O. Robbins. This work was partially supported by the NSF under grants CMMI-1462749, IIP-1362146 (M.O.-S.), CBET-1336634 (K.A.D.), as well as the Taub cluster and Blue Waters resources of NCSA at University of Illinois.

Appendix A: Analysis of the "waiting time"

We study how much more strain is needed to record the next avalanche after an avalanche is observed. The additional strain that is needed is defined as the "waiting time", which we denote by w. Avalanches for a particular system size are considered to occur when the shear stress drop is over 1% of the maximum shear stress drop observed for that system size. The probability distributions of w are plotted in Figure 9 below. Figure 9 shows the distributions are shaped like a plateau followed by an

TABLE IV: Values of scaling exponents. N.A. means the exponents cannot be obtained to a high precision or cannot obtain a good collapse under scaling. The exponents from Refs.[34, 35] are from 2D simulations in the overdamped case. τ is the exponent of the probability distributions. α and β are finite-size-scaling exponents defined in Eq. (11). γ is the exponent for the scaling of the number of avalanches of a given size with the system size. ΔU is defined in Eq. (9) and ΔE is defined in Eq. (7).

Simulations	τ		α		β		γ	
	ΔU	ΔE	ΔU	ΔE	ΔU	ΔE	ΔU	ΔE
Potential I and from our simulations	1.25 ± 0.1	N.A.	1.25 ± 0.05	N.A.	-0.5 ± 0.1	N.A.	1.05 ± 0.1	1.00 ± 0.05
Potential II and from our simulations	1.15 ± 0.1	N.A.	1.2 ± 0.1	N.A.	-0.3 ± 0.1	N.A.	1.15 ± 0.1	1.15 ± 0.1
Potential I and from Refs. [34, 35]	1.3 ± 0.1 [34] and 1.25 ± 0.05 [35]	1.3 [34] and 1.25 [35], with bigger uncertainty than for ΔU	0.9 ± 0.05	0.9 ± 0.05	0.2 ± 0.1	0.2 ± 0.1	1.3 ± 0.1 [34] and 1.3 ± 0.05 [35]	1.3 ± 0.1 [34] and 1.3 ± 0.05 [35]

exponential drop for large "waiting times". After scaling the horizontal and vertical axes, using

$$\frac{P(w)}{L^{\xi}} = h(wL^{\eta}), \tag{A1}$$

where L is the side length of the system, the curves collapse. The value of η can be derived from other scaling exponents that are reported in the paper. To derive η, we notice that the average "waiting time" scales as $\langle w \rangle \sim L^{-\eta}$ according to Eq. (A1) here, which means the total number of events per unit strain interval scales as $n \sim L^{\eta}$. From the paper, $P(\Delta U) \sim L^{\gamma} \Delta U^{-\tau}$. Therefore,

$$n \sim \int_{\Delta U_{min}}^{\Delta U_{max}} L^{\gamma} (\Delta U)^{-\tau} \mathrm{d}(\Delta U) \sim L^{\gamma} \left(\Delta U_{min}^{1-\tau} - \Delta U_{max}^{1-\tau} \right) \tag{A2}$$

As mentioned above, we consider the events that are greater than 1% of the maximum event, i.e. $\Delta U_{min} = 0.01 \Delta U_{max}$. Therefore,

$$n \sim L^{\gamma} \left(\Delta U_{min}^{1-\tau} - \Delta U_{max}^{1-\tau} \right) \sim L^{\gamma} \Delta U_{max}^{1-\tau} \tag{A3}$$

where we assumed $\tau > 1$. Moreover, according to the definition of the scaling exponent α in Eq. (11) of the paper, the maximum event $\Delta U_{max} \sim L^{\alpha}$. Hence,

$$n \sim L^{\gamma} \Delta U_{max}^{1-\tau} \sim L^{\gamma} L^{\alpha(1-\tau)} \tag{A4}$$

i.e.

$$\eta = \gamma + \alpha(1 - \tau) \tag{A5}$$

Using the values of α, τ and γ for ΔU from Table IV of the paper, we get $\eta = 0.74$ for potential I and $\eta = 0.97$ for potential II. Using these values of η and picking proper values for ξ, we see the curves in Figure 9 collapse very well, which serves as a support for the correctness of the simulations.

Appendix B: List of symbols

A list of all symbols used in the paper is shown in Table V.

[1] J. P. Sethna, K. A. Dahmen, and C. R. Myers, Nature **410**, 242 (2001).
[2] A. P. Mehta, K. A. Dahmen, and Y. Ben-Zion, Phys. Rev. E **73**, 056104 (2006).
[3] R. V. Solé and S. C. Manrubia, Phys. Rev. E **54**, R42 (1996).
[4] J. Baró, Á. Corral, X. Illa, A. Planes, E. K. H. Salje, W. Schranz, D. E. Soto-Parra, and E. Vives, Phys. Rev. Lett. **110**, 088702 (2013).
[5] T. Richeton, P. Dobron, F. Chmelik, J. Weiss, and F. Louchet, Mat. Sci. Eng. A **424**, 190 (2006).
[6] B. A. Sun, H. B. Yu, W. Jiao, H. Y. Bai, D. Q. Zhao, and W. H. Wang, Phys. Rev. Lett. **105**, 035501 (2010).
[7] J. L. Ren, C. Chen, G. Wang, N. Mattern, and J. Eckert, AIP Adv. **1**, 032158 (2011).
[8] D. M. Dimiduk, Science **312**, 1188 (2006).
[9] M.-C. Miguel, A. Vespignani, S. Zapperi, J. Weiss, and J.-R. Grasso, Nature **410**, 667 (2001).

TABLE V: List of all symbols used in the paper

Symbol	Meaning
S	Magnitude of avalanches given by stress drops or strain jump sizes
S_c	Cutoff avalanche size
τ	Power-law exponent for the probability distribution of avalanche sizes
τ'	Power-law exponent obtained by fitting the probability distribution of energy drops at avalanches as $P(\Delta E) \sim \Delta E^{-\tau'}$
ΔE	Potential energy drop at an avalanche
L	Side length of the square atomic system domain
$\Delta\sigma$	Shear stress drop at an avalanche
$\Delta\sigma_h$	Hydrostatic pressure drop at an avalanche
A, B	Each represents one of the two atom species in the system
E_{ij}	Potential between an atom of type i and an atom of type j, where i and j can be either A or B
E_0, a_{ij}, E_c	Parameters used in the definition of interatomic potentials given by Eq. (1) and Eq. (2)
r_c	Cutoff distance in the interatomic potential given by Eq. (2)
r	Interatomic distance
N	Number of atoms in the system
E	Potential energy of the system
$\sigma_{xx}, \sigma_{yy}, \sigma_{xy}$	Stress components of the system
$\Delta\epsilon$	Increment of shear strain in each shear step
$(\sigma_h)_i$	Hydrostatic pressure before the i-th shear step
$(\sigma_h)_{i+1}$	Hydrostatic pressure before the $(i+1)$-th shear step, i.e. after the i-th shear step
σ_i	Shear stress before the i-th shear step
σ_{i+1}	Shear stress before the $(i+1)$-th shear step, i.e. after the i-th shear step
E_i	Potential energy in the system before the i-th shear step
E_{i+1}	Potential energy in the system before the $(i+1)$-th shear step, i.e. after the i-th shear step
μ	Shear modulus of the system
A	Area of the system
D	Dimension of the system
$\langle\Delta\sigma_h\rangle$	Average hydrostatic pressure drop for avalanches whose shear stress drops fall within a bin for $\Delta\sigma$
$\Delta\epsilon_{pl}$	Plastic strain accumulated in an avalanche event
$\langle\Delta E\rangle$	Average energy drop for avalanches whose shear stress drops fall within a bin for $\Delta\sigma$
ΔU	A measure of avalanche sizes defined as $\Delta U = \frac{\langle\sigma\rangle\Delta\sigma}{\mu}A$
$\langle\sigma\rangle$	Steady-state shear stress
$P(\cdot)$	Probability distribution function of a quantity
α, β	Exponents for finite-size scaling defined by Eq. (11)
γ	Exponent for the scaling of the number of slip events of a given size with the system size
w	Additional strain needed to record the next avalanche after one avalanche is observed
n	Total number of avalanche events observed when shearing a system by a unit strain in the steady state
ξ, η	Exponents for the "waiting time" scaling defined by Eq. (A1)
ΔU_{max}	Maximum ΔU observed for a particular system size, and also the upper bound of the integration in Eq. (A2)
ΔU_{min}	Lower bound of the integration in Eq. (A2)

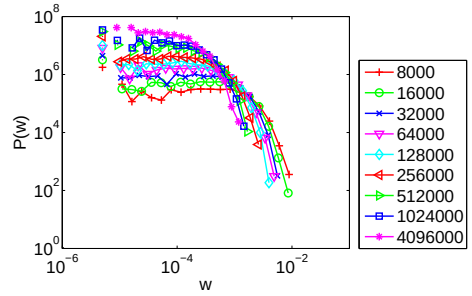

(a)

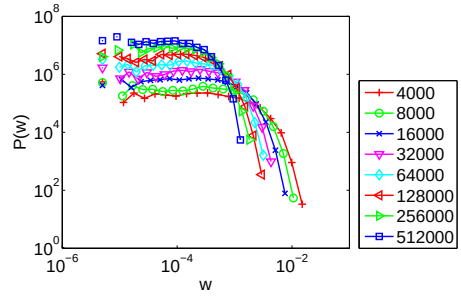

(b)

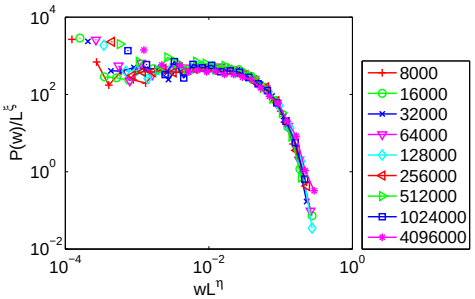

(c)

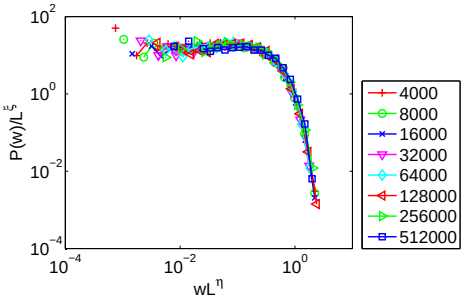

(d)

FIG. 9: $P(w)$ (probability distribution of the "waiting time" w) for different system sizes. The subfigures are (a)$P(w)$ for potential I, (b)$P(w)$ for potential II, (c)scaled $P(w)$ for potential I, where η=0.74 and ξ=1.5, and (d)scaled $P(w)$ for potential II, where η=0.97 and ξ=1.8. L is the side length of the system. ξ and η are scaling exponents shown in Eq. (A1) in this document. The strain increment is 5×10^{-5}. The way of calculating $P(w)$ is such that $P(w) \cdot \mathrm{d}w$ is the number of events that fall in the range $[w, w + \mathrm{d}w]$ per unit strain interval.

[10] N. Friedman, A. T. Jennings, G. Tsekenis, J.-Y. Kim, M. Tao, J. T. Uhl, J. R. Greer, and K. A. Dahmen, Phys. Rev. Lett. **109**, 095507 (2012).

[11] K. A. Dahmen, Y. Ben-Zion, and J. T. Uhl, Nature Physics **7**, 554 (2011).

[12] K. A. Dahmen, Y. Ben-Zion, and J. T. Uhl, Phys. Rev. Lett. **102**, 175501 (2009).

[13] R. Maaß, M. Wraith, J. T. Uhl, J. R. Greer, and K. A. Dahmen, Phys. Rev. E **91**, 042403 (2015).

[14] M. Zaiser and N. Nikitas, J. Stat. Mech. Theor. Exp. **2007**, P04013 (2007).

[15] P. D. Ispánovity, L. Laurson, M. Zaiser, I. Groma, S. Zapperi, and M. J. Alava, Phys. Rev. Lett. **112**, 235501 (2014).

[16] G. Tsekenis, J. T. Uhl, N. Goldenfeld, and K. A. Dahmen, Europhys. Lett. **101**, 36003 (2013).

[17] P. Y. Chan, G. Tsekenis, J. Dantzig, K. A. Dahmen, and N. Goldenfeld, Phys. Rev. Lett. **105**, 015502 (2010).

[18] F. F. Csikor, C. Motz, D. Weygand, M. Zaiser, and S. Zapperi, Science **318**, 251 (2007).

[19] C. A. Schuh, T. C. Hufnagel, and U. Ramamurty, Acta Mater. **55**, 4067 (2007).

[20] B. A. W. Brinkman, M. P. LeBlanc, J. T. Uhl, Y. Ben-Zion, and K. A. Dahmen, Phys. Rev. E **93**, 013003 (2016).

[21] J. Antonaglia, W. J. Wright, X. Gu, R. R. Byer, T. C. Hufnagel, M. LeBlanc, J. T. Uhl, and K. A. Dahmen, Phys. Rev. Lett. **112**, 155501 (2014).

[22] M. LeBlanc, L. Angheluta, K. Dahmen, and N. Goldenfeld, Phys. Rev. E **87**, 022126 (2013).

[23] S. Kale and M. Ostoja-Starzewski, Phys. Rev. Lett. **112**, 045503 (2014).

[24] J. Lin, A. Saade, E. Lerner, A. Rosso, and M. Wyart, Europhys. Lett. **105**, 26003 (2014).

[25] M. Talamali, V. Petäjä, D. Vandembroucq, and S. Roux, Phys. Rev. E **84**, 016115 (2011).

[26] Z. Budrikis and S. Zapperi, Phys. Rev. E **88**, 062403 (2013).

[27] J. Lin, E. Lerner, A. Rosso, and M. Wyart, Proc. Natl. Acad. Sci. U.S.A. **111**, 14382 (2014).

[28] D. S. Fisher, K. Dahmen, S. Ramanathan, and Y. Ben-Zion, Phys. Rev. Lett. **78**, 4885 (1997).

[29] J. Lin and M. Wyart, Phys. Rev. X **6**, 011005 (2016).

[30] C. Maloney and A. Lemaître, Phys. Rev. Lett. **93**, 016001 (2004).

[31] E. Lerner and I. Procaccia, Phys. Rev. E **79**, 066109 (2009).

[32] E. Lerner, N. P. Bailey, and J. C. Dyre, Phys. Rev. E **90**, 052304 (2014).

[33] N. P. Bailey, J. Schiøtz, A. Lemaître, and K. W. Jacobsen, Phys. Rev. Lett. **98**, 095501 (2007).

[34] K. M. Salerno and M. O. Robbins, Phys. Rev. E **88**, 062206 (2013).

[35] K. M. Salerno, C. E. Maloney, and M. O. Robbins, Phys. Rev. Lett. **109**, 105703 (2012).

[36] S. Kobayashi, K. Maeda, and S. Takeuchi, Jpn. J. Appl. Phys. **19**, 1033 (1980).

[37] C. E. Maloney and A. Lemaître, Phys. Rev. E **74**, 016118 (2006).

[38] S. Ogata, F. Shimizu, J. Li, M. Wakeda, and Y. Shibutani, Intermetallics **14**, 1033 (2006).

[39] S. Kobayashi, K. Maeda, and S. Takeuchi, Acta Metall. **28**, 1641 (1980).

[40] C. E. Maloney and M. O. Robbins, Phys. Rev. Lett. **102**, 225502 (2009).
[41] A. Păduraru, A. Kenoufi, N. P. Bailey, and J. Schiøtz, Adv. Eng. Mater. **9**, 505 (2007).
[42] Y. Q. Cheng, E. Ma, and H. W. Sheng, Phys. Rev. Lett. **102**, 245501 (2009).
[43] C. E. Maloney and M. O. Robbins, J. Phys. Condens. Matter **20**, 244128 (2008).
[44] T. Zhu and E. Ertekin, Phys. Rev. B **93**, 155414 (2016).
[45] T. Zhu and E. Ertekin, Nano Lett. **16**, 4763 (2016).
[46] B. Tadmor, Ellad and R. E. Miller, *Modeling Materials: Continuum, Atomistic and Multiscale Techniques*, 1st ed. (Cambridge University Press, Cambridge: New York, 2012).
[47] A. C. Lund and C. A. Schuh, Acta Mater. **51**, 5399 (2003).
[48] K. Maeda and S. Takeuchi, Philos. Mag. A **44**, 643 (1981).
[49] Q.-K. Li and M. Li, Appl. Phys. Lett. **88**, 241903 (2006).
[50] A. Cao, Y. Cheng, and E. Ma, Acta Mater. **57**, 5146 (2009).
[51] W. Wright, T. Hufnagel, and W. Nix, J. Appl. Phys. **93**, 1432 (2003).
[52] J. Li, F. Spaepen, and T. C. Hufnagel, Philos. Mag. A **82**, 2623 (2002).
[53] J. Li, Z. L. Wang, and T. C. Hufnagel, Phys. Rev. B **65**, 144201 (2002).
[54] Y. Wei, A. F. Bower, and H. Gao, Phys. Rev. B **81**, 125402 (2010).
[55] J. Lin, T. Gueudré, A. Rosso, and M. Wyart, Phys. Rev. Lett. **115**, 168001 (2015).